Archives of Acoustics Vol. 50, No. 4, pp. 501–512 (2025), https://doi.org/10.24425/aoa.2025.156931

Research Paper

Simulation Analysis of Beam Intensity Attenuation Patterns and Source Depth Estimation Using a Vertical Long Line Array

Hao WANG, Guangying ZHENG*, Fangwei ZHU, Xiaohong YANG, Shuaishuai ZHANG, Xiaowei GUO

Hangzhou Applied Acoustics Research Institution
Hangzhou, China

*Corresponding Author e-mail: 276454158@qq.com

Received May 29, 2025; revised September 30, 2025; accepted October 8, 2025; published online November 17, 2025.

In the deep-water reliable acoustic path (RAP), when estimating target depth using a vertical array, a large-aperture array can enhance the extraction of the acoustic field interference structure under low signal-to-noise ratio (SNR). However, this operation introduces slow envelope modulation (the envelope amplitude of peak beam intensity decreases with frequency) to the broadband acoustic field interference pattern, significantly degrading the performance of estimating the source depth. The Kraken normal-mode model can accurately calculate low-frequency sound fields in deep-water environments. This paper uses this tool to find that, in the deep-water direct arrival zone (DAZ), the peak beam intensity output of a vertical linear array varies across a broadband frequency range, exhibiting a pattern combining periodic changes of Lloyd's mirror interference and inherent envelope attenuation changes. The physical mechanism of envelope attenuation is explained through both theoretical derivation and simulation analysis, key factors affecting the envelope-attenuation pattern are clarified, and the impact of beam-intensity envelope attenuation on the depth-estimation method based on matched beam intensity processing (MBIP) is pointed out. Based on this, a modified target depth estimation method of matched beam intensity processing (M-MBIP) that contains an attenuation coefficient is proposed, and its effectiveness is verified through simulated data.

Keywords: deep-water direct arrival zone (DAZ); Lloyd's mirror interference; broadband attenuation pattern; source depth estimation.

1. Introduction

Three-dimensional acoustic target localization involves the estimation of azimuth, range, and depth, with target depth being a key indicator for surface and underwater target identification (Gaul *et al.*, 2007). Recently, underwater target depth estimation has gained significant attention from acousticians.

As a typical sound propagation mode in deep water, the reliable acoustic path (RAP) propagation mode is widely used for target detection in the upper water column (typically within 200 m from the surface). RAP-based target localization has two main advantages. First, the grazing angle of the received signal measured by a vertical array can be used to estimate the target range. Second, the acoustic signal radiated by a near-sea surface source propagates to a near-seabed receiver through the reliable acoustic path. The acoustic signal of the receiver mainly comes from the superposition of the direct acoustic signal and the sea surface-reflected acoustic signal, forming a typical Lloyd's mirror interference effect that produces distinct interference fringes in the acoustic field. These fringes are highly sensitive to changes in source depth (Worcester *et al.*, 2013). Due to these advantages, using Lloyd's mirror interference for estimating source depth has attracted extensive research (McCargar, Zurk, 2013; Li *et al.*, 2022; Duan *et al.*, 2012; Wei *et al.*, 2020).

McCargar and Zurk (2012) were the first to explore the use of Lloyd's mirror interference for estimating source depth, showing that for narrowband sig-

nals, acoustic intensity, as a function of range, is modulated by source depth. They proposed the generalized Fourier transform (GFT) method for depth estimation. Kniffin *et al.* (2016) later provided a theoretical analysis of the GFT method's performance and introduced a more straightforward depth-estimation technique based on the spacing of beam-intensity nulls. Lei *et al.* (2016) presented a passive source localization method that uses deep-water multipath RAP and cross-correlation matching for localizing source. Xu *et al.* (2023), addressing the performance degradation in GFT implementation in real-world deep-water environments, designed a preprocessing resampling scheme that enhances the periodicity of beam intensity in the grazing angle sine domain and improves depth-estimation accuracy when applied to GFT.

Zheng *et al.* (2020) pointed out that GFT is a typical non-perfect match from the generalized matched-field processing perspective. They proposed the matched beam intensity processing method (MBIP), an incoherent processing technique that matches data-beam intensity variations with those of assumed source depth, achieving better accuracy for near-surface source. Based on the research of Zheng *et al.* (2020), Zhou *et al.* (2022) proposed a depth estimation method that matches the interference structure in the frequency domain for narrowband source-depth estimation. This method can be used for real-time or semi-real-time source-depth estimation and classification. Wang *et al.* (2021) presented a broadband source-depth estimation method using the frequency-grazing angle interference structure to distinguish multiple underwater targets, validated by both simulation and experimental data.

The aforementioned methods and experiments were conducted using a pressure hydrophone array, while a vector hydrophone can simultaneously measure both acoustic pressure and particle velocity at the same point in the acoustic field. Zhang *et al.* (2025) addressed the passive detection problem using deep-water vector vertical arrays in a RAP environment, and proposed a coherent matched broadband complex acoustic intensity interference pattern (CM-BCAIIP) method for shallow-target depth estimation with high real-time capability. Sun *et al.* (2016) studied the distribution characteristics of the RAP vector acoustic field and estimated the range using derived from angle-of-arrival information from the horizontal and vertical components of complex acoustic intensity (see also, Zhu, Sun, 2023).

Whether using pressure-field or vector-field broadband interference structures for target- depth estimation in RAP, a low signal-to-noise ratio (SNR) causes large errors in the acoustic-field broadband interference structure extraction. This leads to poor performance in target-depth estimation. Although increasing the array aperture can increase array processing gains and improve the SNR of tracking beams, thereby enhancing the extraction of the broadband interference structure, this approach introduces slow envelope modulation. This causes the peak beam intensity to decay with frequency, which can significantly degrade the performance of traditional target-depth estimation methods.

To address this, this paper reviews Lloyd's mirror interference theory, pointed out the fast calculation equation for peak beam intensity, the attenuation law of peak beam intensity under vertical long array was briefly analyzed (which will be verified later), and based on this law proposes a M-MBIP method based on the MBIP approach. It then utilizes the Kraken normal-mode model to accurately compute the acoustic field at low-frequency (usually below 500 Hz) in the deep sea. This enables to analyze the key factors and patterns causing broadband attenuation of beam intensity through theory and simulation. Finally, simulation results are used to confirm that the proposed M-MBIP method is superior to the conventional MBIP method.

1.1. Lloyd's mirror interference theory

Duan *et al.* (2012) presented the conventional beamforming (CBF) output of a near-bottom vertical line array (VLA) arranged as shown in Fig. 1 (see also, Zhu *et al.*, 2021), under the assumption of a constant sound speed:

$$P(\omega, z_s, z_j) \approx -2iS(\omega)\frac{e^{ikR}}{R_s}\sin(kz_s \sin\theta_S), \tag{1}$$

$$B(\omega, \sin\theta, z_s) = \left|\sum_{n=1}^{N} e^{jk(nd-\overline{z})\sin\theta} P(\omega, z_s, z_j)\right|^2, \tag{2}$$

where N represents the number of array elements, d represents the spacing between array elements, $\overline{z}$ is the depth of the VLA center, θ is the grazing angle of the sound signal, $S(\omega)$ denotes the source strength, $P(\omega, z_s, z_j)$ represents the complex sound pressure received by the j-th hydrophone, $B(\omega, \sin\theta, z_s)$ is the beam intensity obtained after applying CBF to the complex sound pressure field recorded by the VLA, $\omega = 2\pi f$ is the angular frequency of the acoustic wave,

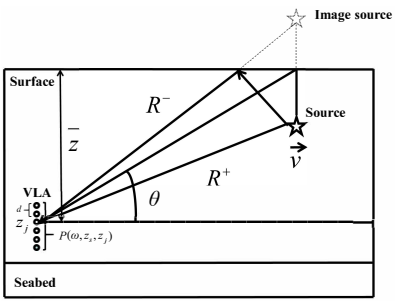

Fig. 1. Diagram of the source and vertical line array (VLA) geometry.

$k = k(\omega)$ is the wavenumber of the acoustic wave, z_j denotes the receiving depth of the j-th hydrophone, z_s is the source depth, $R_s = \sqrt{R^2 + z_j^2}$, R is the horizontal range between the source and the VLA, and $\sin\theta_S = \frac{\bar{z}}{\sqrt{\bar{z}^2+R^2}}$.

When the signal's detected grazing angle is θ_s, the peak beam intensity B can be expressed as (Zheng *et al.*, 2020):

$$B(\omega, \sin\theta_s, z_s) = 2\frac{|S(\omega)|^2}{\bar{z}^2}\sin^2\theta_s \cdot [1 - \cos(2kz_s\sin\theta_s)]. \quad (3)$$

Equation (3) represents the beam intensity under a constant sound speed. In the actual process of sound propagation, the change in the sound speed gradient causes acoustic ray refraction. The equation of peak beam intensity considering the bending of acoustic rays is as follows:

$$B(\omega, \sin\theta_s, z_s) = 2\frac{|S(\omega)|^2}{\bar{z}^2}\sin^2\theta_s \cdot \left[1 - \cos\left(2kz_s\sqrt{c_r^2/\bar{c}^2 + \sin\theta_s^2 - 1}\right)\right], \quad (4)$$

where c_r is the sound speed at the receiving depth, and $\bar{c}$ is the equivalent sound speed from the sea surface to the source depth, expressed as

$$\bar{c} = \sqrt{\left(z_s \Big/ \int_0^{z_s} 1/c^2(z)\,\mathrm{d}z\right)}. \quad (5)$$

Then, the frequency interference period of the peak beam intensity, considering the refraction of sound rays, can be expressed as

$$\Delta f_{\mathrm{PD}} \approx \frac{c_r}{2z_s\sqrt{c_r^2/\bar{c}^2 + \sin\theta_s^2 - 1}}. \quad (6)$$

It is clear from this formulation that the change of beam intensity with frequency is periodic whether under constant sound speed or varying sound speed. Therefore, the behaviour of beam intensity variation under broadband conditions can be studied based on either case.

1.2. Broadband modified MBIP target depth estimation method (M-MBIP)

Under the Lloyd's mirror interference theory, the MBIP method proposed in (Zheng *et al.*, 2020) is based on a small-aperture VLA. It constructs replica beam intensity time series (referred to as replica envelopes) at different depths and matches them with the actual output beam intensity time series from the array (referred to as data envelopes) to estimate the source depth. This process is completed through a fuzziness function similar to Eq. (10). The replica envelopes are calculated using Eq. (3). However, for large-aperture VLAs, the peak beam intensity attenuates with frequency increases after beamforming. In this case, the replica envelope calculated by Eq. (3) does not match the actual value, and using the MBIP method can lead to erroneous depth estimates. To solve this, this paper proposes a modified target depth estimation method based on the MBIP method, as detailed further.

When the target source is within 5 km of the VLA, the Kraken program (Porter, 1991) can be used. In the simulated marine environment, attenuated replica envelopes for different source depths can be calculated. By matching these attenuated replica envelopes with the data envelopes, the target depth can be estimated. For target sources at a range of 5 km–15 km from the array, the peak attenuation of its replica envelope is close to a constant value. By using Kraken to calculate the envelope attenuation coefficient of the replica at any of the above ranges and substituting it into Eq. (3), an approximate attenuated replica envelope can be obtained. Matching this approximate replica with the data envelope can quickly provide the target source depth while reducing computation time. The main steps of the proposed method are as follows:

1) estimate the target range r_e based on the VLA measurement of signal's arrival grazing angle θ_r;
2) for the given deep water environment, assuming a frequency band $\omega \in [\omega_l, \omega_h]$, array depth $z_r \in [z_{r1}, z_{rN}]$, target range r_e, and target depth $z_s \in [z_{s1}, z_{sN}]$, generate the broadband sound field $p(\omega; r_e, z_s, z_r)$ at a certain array element based on Kraken;
3) when the target depth $z_s = z$, the sound field matrix of the entire array can be represented as

$$\mathbf{p} = \left[p\left(\omega; r_e, z, z_r^{(1)}\right), p\left(\omega; r_e, z, z_r^{(2)}\right), ..., p\left(\omega; r_e, z, z_r^{(N)}\right)\right]^{\mathrm{T}}; \quad (7)$$

4) when the arrival grazing angle is θ_r, the peak beam intensity I of the array can be calculated as

$$I(\omega; z; \sin\theta_r) = \mathbf{w}'\mathbf{p}\mathbf{p}'\mathbf{w}, \quad (8)$$

where w is the steering vector for beamforming, which incorporates the spacing d between array components. The steering vector w (incorporating the spacing d between array components) is defined as

$$\mathbf{w} = \left[1, e^{jkd\sin\theta_r}, ..., e^{jk(N-1)d\sin\theta_r}\right]^{\mathrm{T}}; \quad (9)$$

5) calculate the ambiguity function of the broadband modified MBIP target depth estimation method by matching the peak beam intensity time series measured from data against a replica peak beam intensity time series evaluated for an assumed source depth, where its peak can be regarded as the real depth of the source:

$$M_{M-\mathrm{MBIP}}(z)=\begin{cases}\dfrac{\int_{\omega_l}^{\omega_h} I_{rp1}(\omega;z;\sin\theta_r)I_{\mathrm{data}}(\omega;z;\sin\theta_r)\,\mathrm{d}\omega}{\sqrt{\int_{\omega_l}^{\omega_h}|I_{rp1}(\omega;z;\sin\theta_r)|^2\,\mathrm{d}\omega}\sqrt{\int_{\omega_l}^{\omega_h}|I_{\mathrm{data}}(\omega;z;\sin\theta_r)|^2\,\mathrm{d}\omega}} & (r<5\,\mathrm{km}),\\ \dfrac{\int_{\omega_l}^{\omega_h}(1+\mu*\Delta f)I_{rp1}(\omega;z;\sin\theta_r)I_{\mathrm{data}}(\omega;z;\sin\theta_r)\,\mathrm{d}\omega}{\sqrt{\int_{\omega_l}^{\omega_h}|(1+\mu*\Delta f)I_{rp1}(\omega;z;\sin\theta_r)|^2\,\mathrm{d}\omega}\sqrt{\int_{\omega_l}^{\omega_h}|I_{\mathrm{data}}(\omega;z;\sin\theta_r)|^2\,\mathrm{d}\omega}} & (5\,\mathrm{km}\le r<5\,\mathrm{km}),\end{cases} \tag{10}$$

where I_{rp1} denotes the replica envelope, I_{data} denotes the data envelope, μ is the attenuation coefficient of the envelope, and Δf is the frequency interval.

Similar to MBIP, the depth corresponding to the peak of the ambiguity function is the estimated target depth.

2. Research and analysis of beam intensity broadband attenuation pattern

This section studies the mechanisms responsible for the attenuation of peak beam intensity in deep-water, large-aperture VLAs. It also analyzes the patterns of beam intensity attenuation under variations in array aperture, source depth, and other related factors.

2.1. Sound field interference structure for a long VLA

To reasonably analyze the factors influencing the extracted envelope of the sound field interference structure from a VLA, simulations are conducted using the Kraken normal-mode acoustic field calculation program. The simulation adopts a Munk sound speed profile typical of deep water, as shown in Fig. 2, with a critical depth of 4800 m. A 128-element VLA is laid near the seabed, with an element spacing of 5 m, the first element located at a depth of 4315 m and the last element at 4950 m, giving a total array aperture of 635 m.

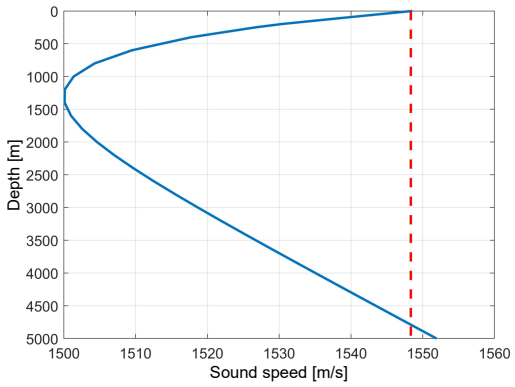

Fig. 2. Deep-water Munk sound speed profile.

In the simulation, the source is set at a depth of 50 m and a horizontal range of 7 km. Broadband array data spanning from 50 Hz to 200 Hz is generated using the Kraken program. CBF is applied to the received VLA data. The results are shown in Fig. 3, where display peaks (red stripes) correspond to the grazing angles of signal arrivals. Positive and negative values correspond to waves arriving from the sea surface and seabed directions, respectively. The peak beam exhibits pronounced interference in the frequency dimension.

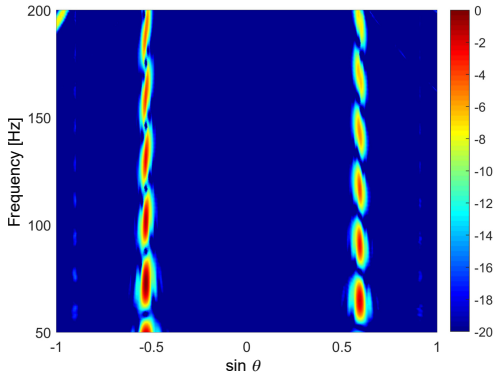

Fig. 3. Conventional beamforming output as a function of grazing angle and frequency.

The peak beam intensity at a grazing angle sine (+0.59) is extracted from Fig. 3 and shown in Fig. 4. It can be seen that the peak beam intensity changes periodically with frequency, while the envelope of the peak shows an almost linear attenuation. This attenuation pattern can lead to incorrect target depth estimation in MBIP, which could cause the omission of information necessary for target depth identification.

To explore the cause of the peak beam intensity attenuation, Fig. 5 shows the broadband transmission loss at different receiver depths corresponding to the source.

As shown in Fig. 5, the energy peaks correspond to two frequency points: 190 Hz (high-frequency) and

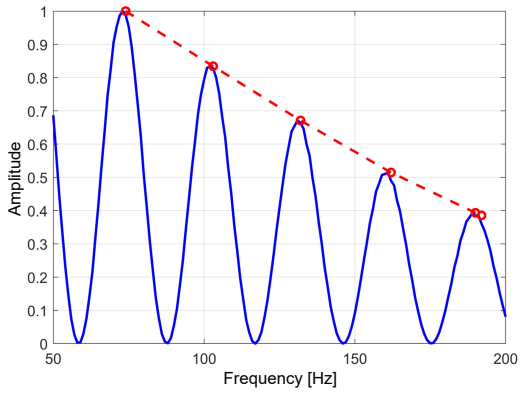

Fig. 4. Peak beam intensity variation with frequency (red dashed line in the figure shows the attenuation trend of the peak).

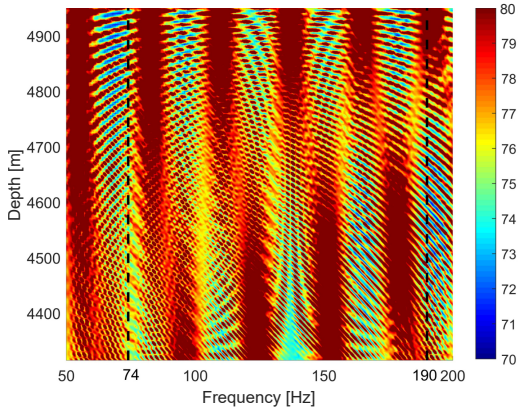

Fig. 5. Transmission loss at different depths.

74 Hz (low-frequency). Figure 6 further illustrates the variation of transmission loss with receiver depth. It is observed that the transmission loss at 74 Hz remains relatively stable across depths, whereas at 190 Hz, the transmission loss progressively increases with depth, leading to a gradual attenuation of beam energy. This phenomenon results in a reduction of peak beam intensity as frequency rises.

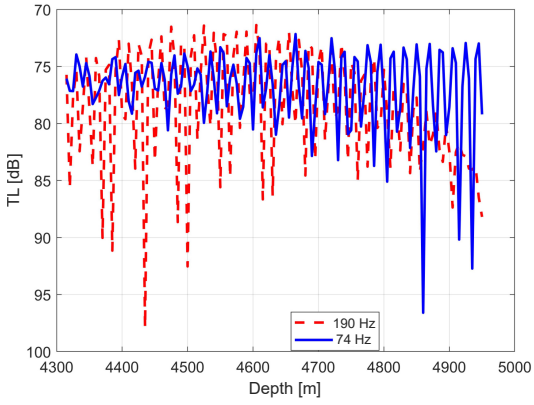

Fig. 6. Transmission loss of sound propagation at different frequencies.

It is evident that the transmission loss of high-frequency acoustic signals increases with depth. This is the main reason for the attenuation of peak beam intensity with frequency after beamforming using a long VLA.

2.2. Influence of array aperture on beam intensity attenuation pattern

In the simulation environment described in Subsec. 2.1, with the array element spacing and the depth of the first array element kept constant, CBF is performed for different array apertures: 32, 64, 96, and 128 elements. The resulting variation of peak beam intensity with range and frequency is shown in Fig. 7.

Observing the energy variation from low to high frequency in Fig. 7, it can be seen that at the same range, as the frequency increases, the peak beam intensity fluctuates periodically. Additionally, as the array aperture increases, the energy attenuation with frequency becomes faster. Figure 8 shows the variation of peak beam intensity with frequency at different ranges for 64 and 128 array elements. Comparing the two subfigures in Fig. 8, it can be seen that after 5 km, the peak beam intensity at high frequencies for 128 array elements is significantly lower than that for 64 array elements, and the peak attenuation is close to linear, as shown by the red dashed curve, while the red circles indicate the extremes.

2.2.1. Linear attenuation coefficient

To quantify the attenuation pattern of beam intensity across broadband frequencies, an in-band linear attenuation coefficient is defined, with the calculation method as follows (the μ in this section corresponds to the same variable previously defined in Subsec. 1.2):

$$\mu = \left(A_{h_p} - A_{l_p}\right) / \left(f_{h_p} - f_{l_p}\right), \tag{11}$$

where, assuming there are multiple extreme points in a frequency band of 50 Hz–200 Hz, A_{h_p} is the value of the last extreme point, A_{l_p} is the value of the first extreme point, f_{h_p} is the frequency corresponding to the last extreme point, and f_{l_p} is the frequency corresponding to the first extreme point.

The linear attenuation coefficients for the 64-element and 128-element arrays are calculated and shown in Fig. 9. It can be seen that the linear attenuation coefficient μ is related to the target range, with around 5 km acting as a critical point. When the range is less than 5 km, μ fluctuates greatly. When the range is greater than 5 km, it varies within a certain range. Moreover, the larger the array aperture, the greater the absolute value of μ, indicating that the beam intensity attenuates more rapidly with frequency change. This observation also confirms the effect of depth-dimension extension on peak beam intensity, as mentioned in Subsec. 2.1.

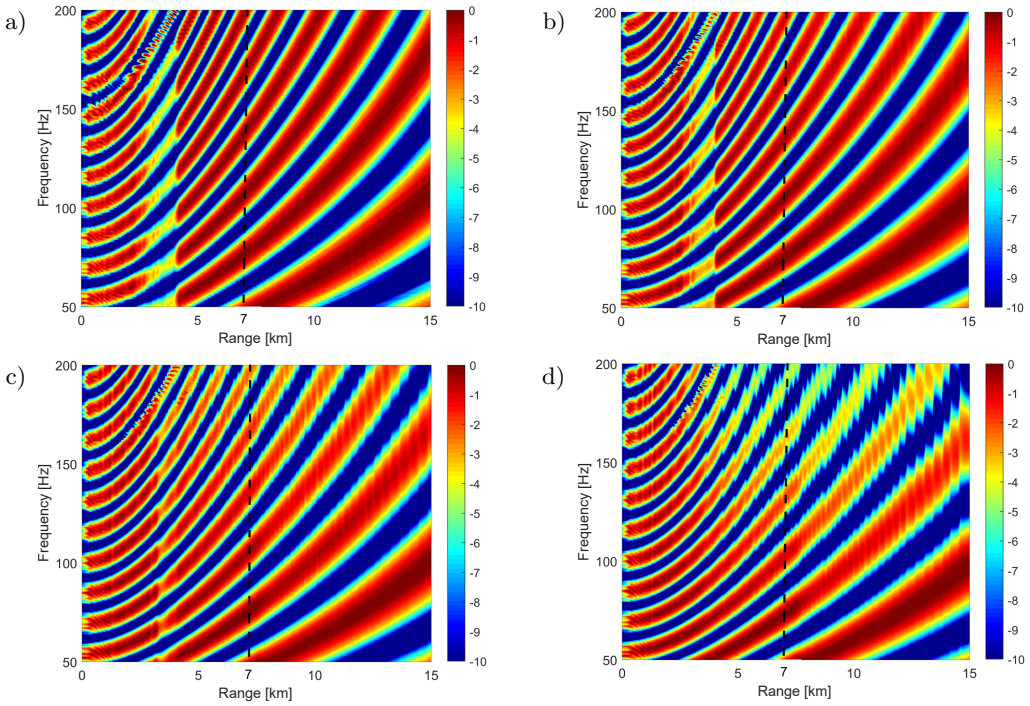

Fig. 7. Variation of peak beam intensity with range and frequency for different array apertures: a) 32 array elements; b) 64 array elements; c) 96 array elements; d) 128 array elements.

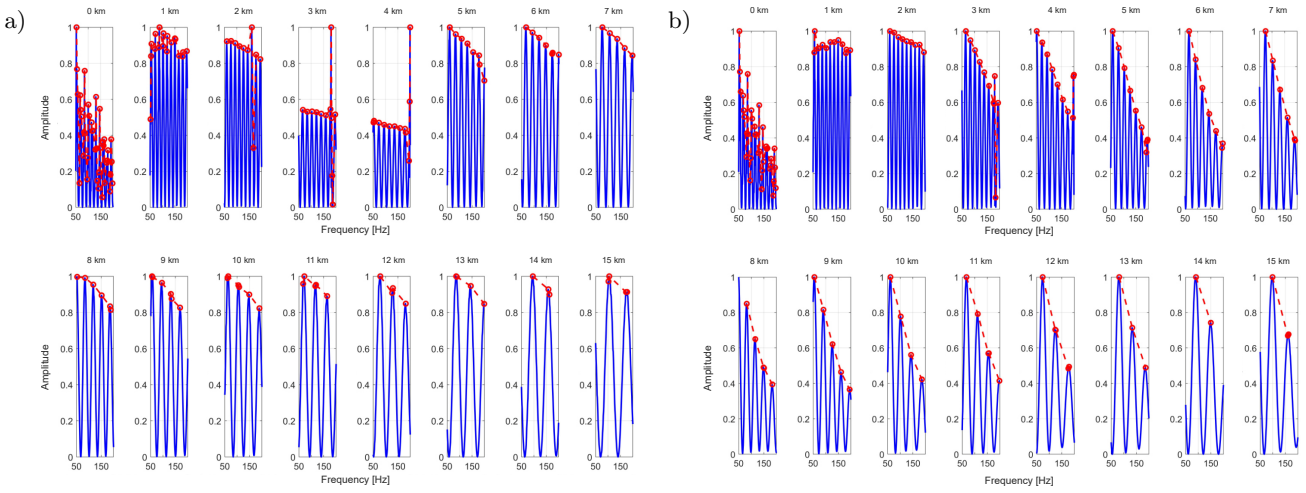

Fig. 8. Variation of peak beam intensity with frequency at different array apertures and horizontal ranges: a) 64 array elements; b) 128 array elements.

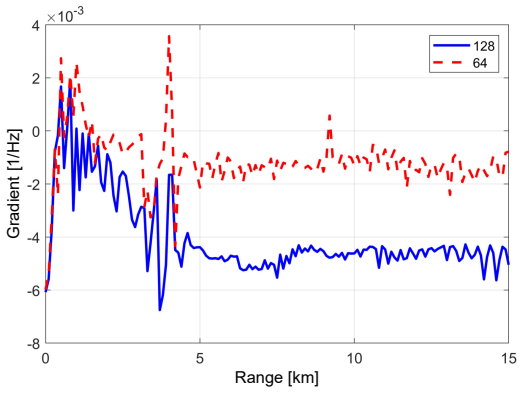

Fig. 9. Variation of linear attenuation coefficient with target range.

2.3. Influence of source depth on beam intensity attenuation pattern

Under the same simulation conditions and procedures as described in Subsec. 2.1, the source depth was varied at 50 m, 100 m, and 200 m. The variations of peak beam intensity as functions of range and frequency are presented in Fig. 10.

From Fig. 10, it can be observed that, at the same range, as the frequency increases, the peak beam intensity fluctuates periodically, the number of interference fringes increases significantly, and the amplitude of the energy gradually decreases.

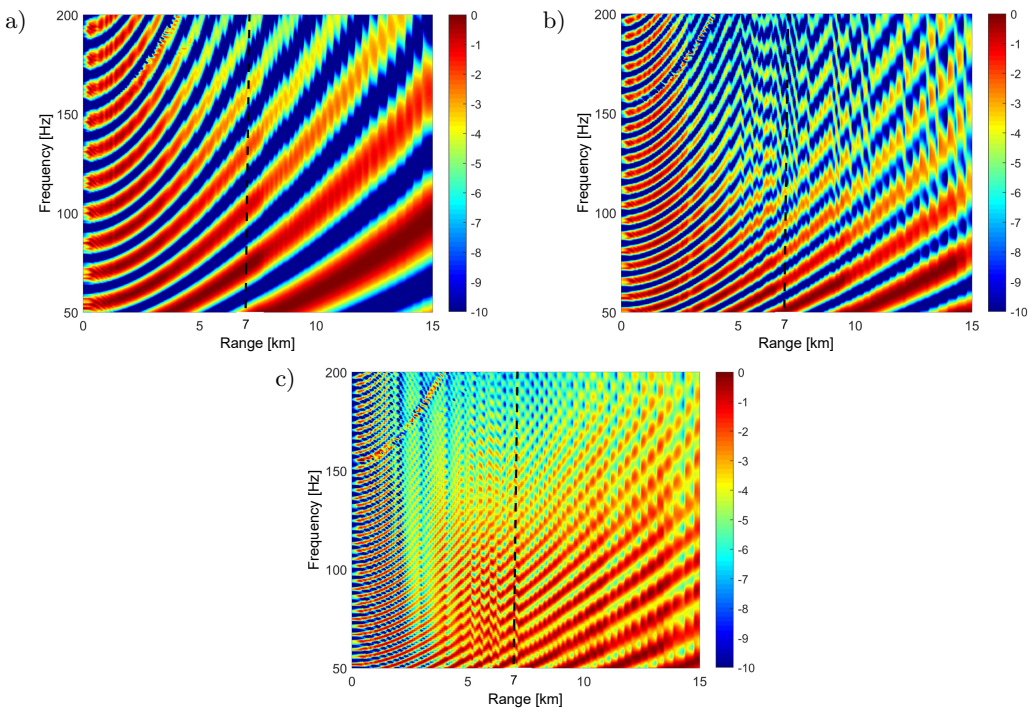

Fig. 10. Variation of peak beam intensity with range and frequency at target depths of: a) 50 m; b) 100 m; c) 200 m.

Furthermore, the peak beam intensity at a range of 7 km under different source depth conditions is obtained, and its variation with frequency is shown in Fig. 11.

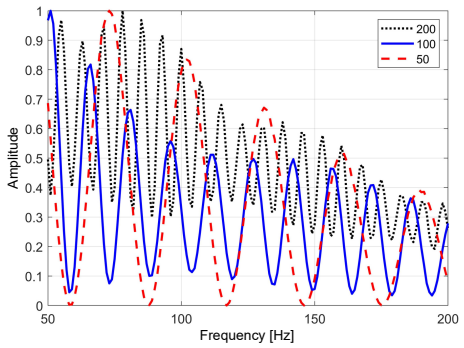

Fig. 11. Variation of peak beam intensity with frequency at 7 km range for different source depths.

It can be seen from Fig. 11 that as the source depth increases, the period of the sound field interference shortens and the number of interference fringes increases, which is consistent with the analysis shown in Fig. 10. The linear attenuation coefficients corresponding to different source depths are calculated, and the results are presented in Fig. 12. It can be seen that as the source depth increases, the absolute value of the attenuation coefficient decreases slightly, while the attenuation trends of different source depths are basically the same. The absolute value of the attenuation coefficient gradually increases within a range of 5 km, and beyond 5 km, it tends to a constant value.

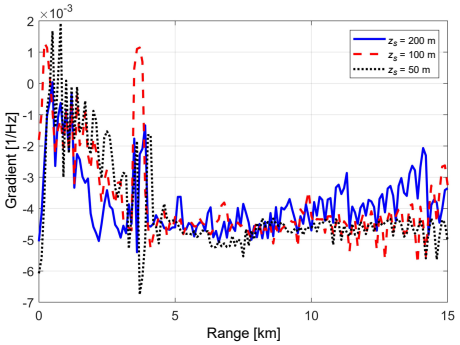

Fig. 12. Variation of linear attenuation coefficient with target for different target depths.

2.4. Influence of array depth on beam intensity attenuation pattern

This section analyzes the broadband attenuation pattern of beam intensity when the array deployment depth varies. Using the same simulation conditions as in Subsec. 2.1, the deployment depth of the array is varied by changing the depth of the 128-th element to 3950 m, 4450 m, and 4950 m. The variation of the peak beam intensity with range and frequency is shown in Fig. 13.

From Fig. 13, it can be seen that at the same range, the peak beam intensity fluctuates periodically from low to high frequency. However, as the array deployment depth increases, there is no obvious trend in the energy attenuation rate. Figure 14 further shows the variation of peak beam intensity with frequency at a range of 7 km for different array deployment depths.

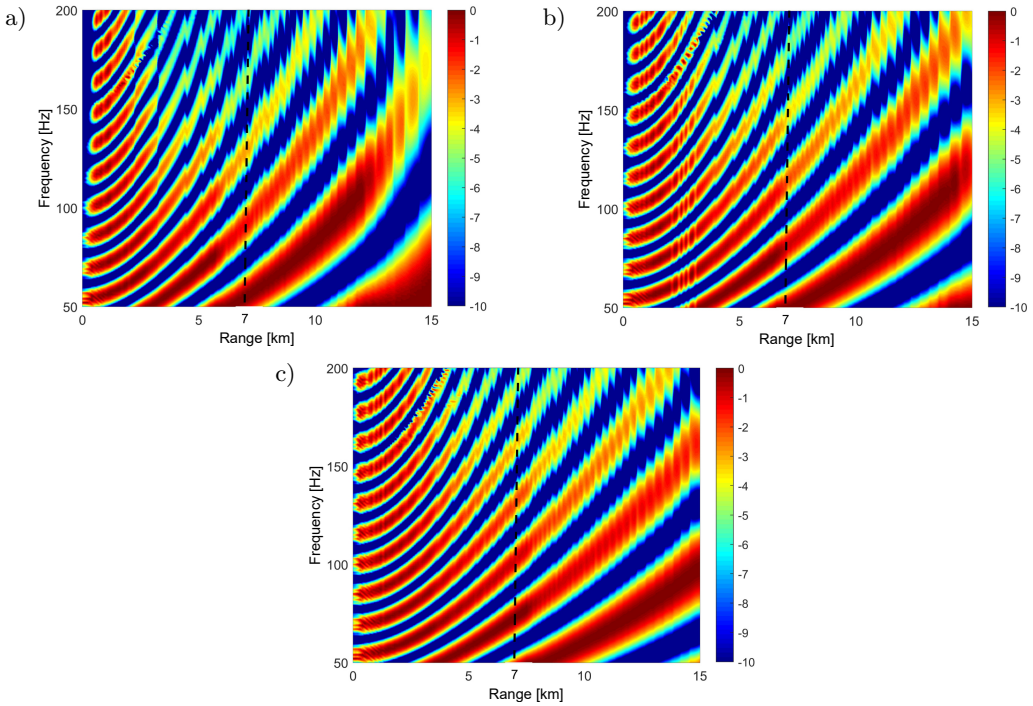

Fig. 13. Variation of peak beam intensity with range and frequency at different array deployment depths: a) 3950 m; b) 4450 m; c) 4950 m.

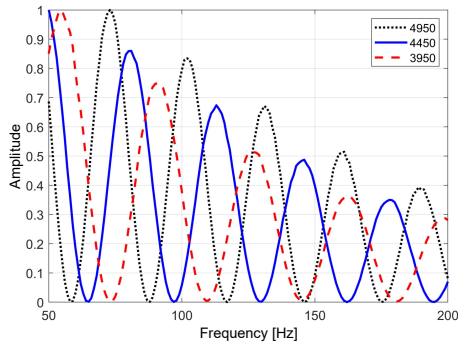

Fig. 14. Variation of peak beam intensity with frequency at 7 km range for different array deployment depths.

It can be seen from Fig. 14 that the attenuation trends of the peak beam intensities at 7 km under different source depths are basically the same. The linear attenuation coefficients corresponding to different array deployment depths are calculated, as shown in Fig. 15. It can be seen that the attenuation trends of the beam intensity under different array deployment depths remain basically the same, although the absolute value of the linear attenuation coefficient decreases as the deployment depth of the array increases.

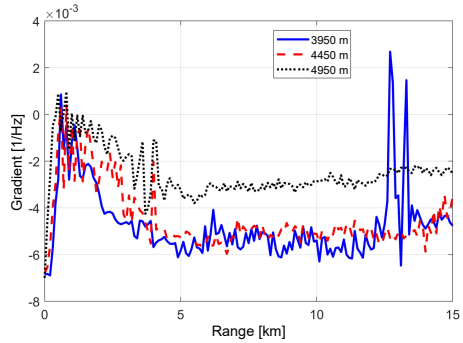

Fig. 15. Variation of linear attenuation coefficient with target range for different array deployment depths.

2.5. Influence of sound speed profile on beam intensity attenuation pattern

Given the unique characteristics of the deep-water DAZ, this study compares isovelocity (1510 m/s) with Munk sound speed profiles to illustrate the influence of the sound-speed profile on the broadband beam intensity attenuation pattern.

Except for setting the sound-speed gradient as a constant sound speed, the same simulation conditions are adopted as those in Subsec. 2.1. After generating broadband array data with Kraken and performing conventional beamforming, the peak beam intensity envelopes at different ranges are shown in Fig. 16.

Compared with Fig. 8b, when the range between the source and array is greater than 5 km, the beam intensity envelope shows nearly linear attenuation within 50 Hz–200 Hz.

Figure 17 further illustrates the variation of linear attenuation coefficients with range for both isovelocity and Munk profiles, showing similar trends in both cases.

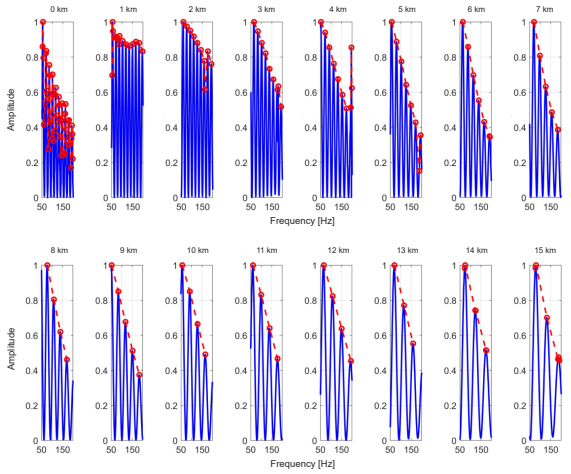

Fig. 16. Variation of peak beam intensity with range under constant sound speed.

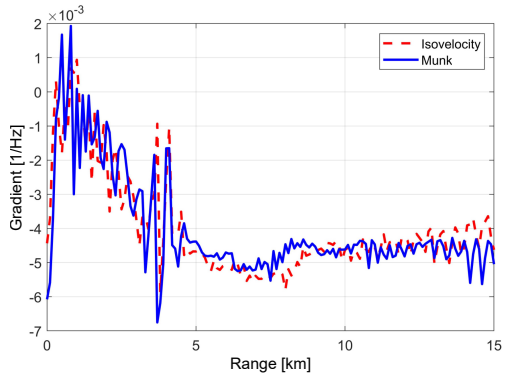

Fig. 17. Variation of linear attenuation coefficient with target range under profiles – isovelocity and Munk sound speed.

3. Simulation results for target depth estimation

To verify whether the depth-estimation performance of the M-MBIP method under a long VLA is better than that of the MBIP method, the Kraken program is used for simulation. The simulation selects a typical Munk sound channel, sets the source depths to 50 m, 100 m, and 150 m. The receiving array is a 128-element VLA, the depth of the first element is at 4315 m and an element spacing is 5 m. The corresponding center frequency is at 125 Hz, the receiving range is at 7 km, and Gaussian white noise with an SNR of −10 dB is added to the VLA data. After conventional beamforming, the results are presented in Fig. 18.

As known from Subsec. 2.1, the peak beam intensity at the sine of the grazing angle in Fig. 18 corresponds to waves incoming from the sea surface, which is used as the replica envelope of the M-MBIP method. At the same time, the replica envelope of the MBIP method is generated using Eq. (3), and both are compared with the data envelope of the array output (see Fig. 19).

It can be seen in Fig. 19 that the data envelope is basically covered within the envelopes of both M-MBIP and MBIP, but the envelope of M-MBIP has a higher degree of coincidence with the data envelope.

The source depth is estimated using the M-MBIP method and the MBIP method, as shown in Fig. 20.

It can be seen from Fig. 20 that the depth-estimation ambiguity function of the M-MBIP and

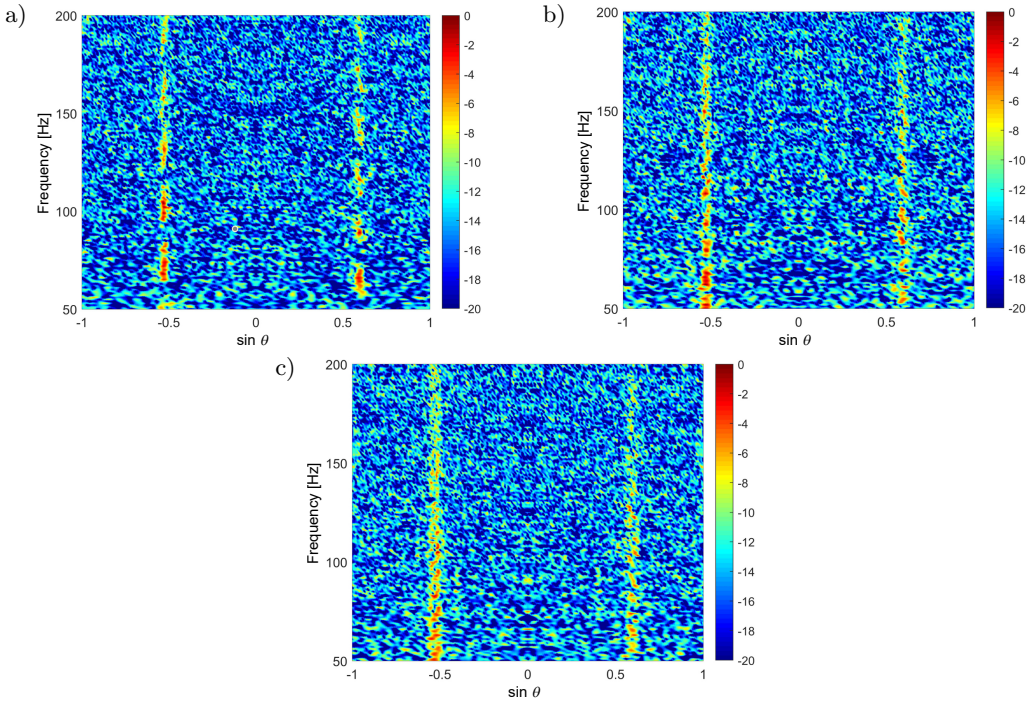

Fig. 18. Conventional beamforming output with an SNR of −10 dB at different source depths: a) z_s = 50 m; b) z_s = 100 m; c) z_s = 150 m.

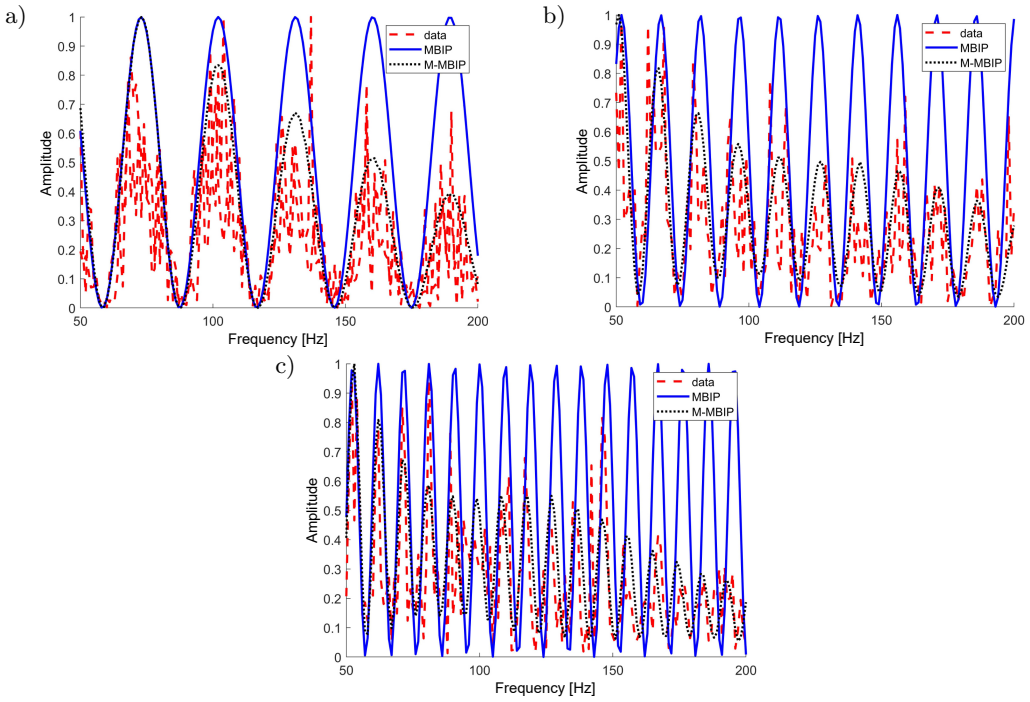

Fig. 19. Interference envelopes of beam energy for different source depths: a) z_s = 50 m; b) z_s = 100 m; c) z_s = 150 m.

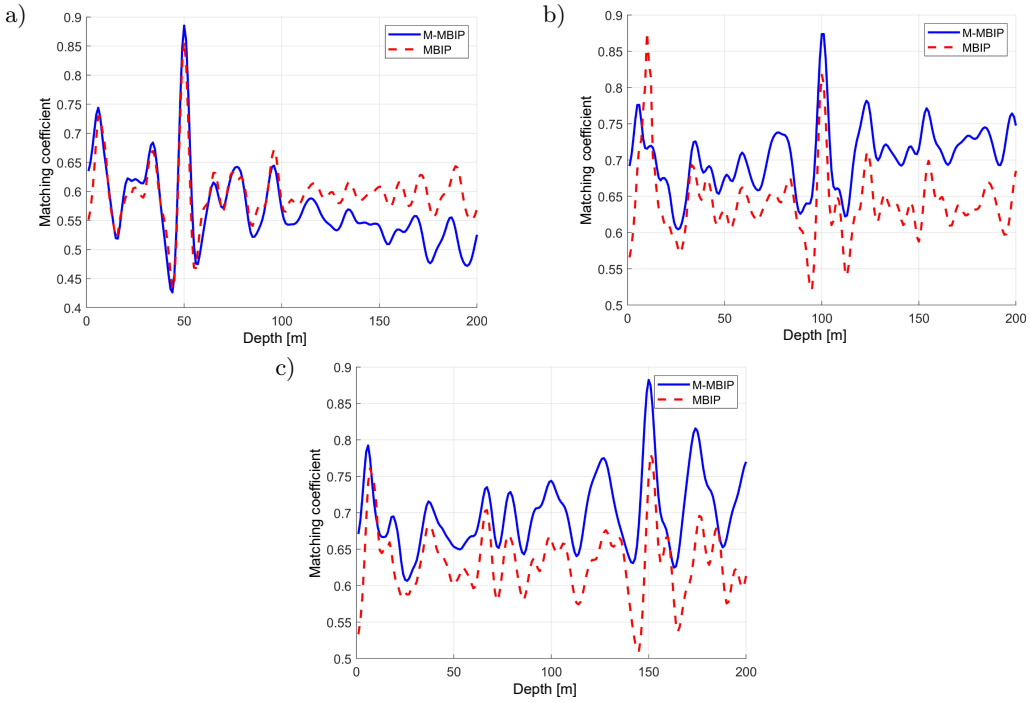

Fig. 20. Comparison of M-MBIP and MBIP methods for different source depths: a) z_s = 50 m; b) z_s = 100 m; c) z_s = 150 m.

MBIP methods have similar estimation capabilities when the source depth is 50 m. The peak of the M-MBIP method at the true depth is slightly higher than that of the MBIP method; when the source depth is 100 m or 150 m, the MBIP method performs poorly, with false peaks appearing at shallow depths, resulting in depth misjudgment problems. However, the peak of the M-MBIP method at the true source depth is always higher than that of the MBIP method, and no false peaks appear. Therefore, the depth-estimation performance of the M-MBIP method under a long VLA is better than that of the MBIP method.

4. Conclusion

This paper examined the issue of slow envelope modulation in the broadband interference structure of large-aperture VLA in deep water DAZ, which degrades source depth estimation. Through theoretical and simulation analyses, the key factors affecting the attenuation of peak beam intensity were identified, and a modified M-MBIP method based on MBIP was proposed. There are several conclusions that can be drawn:

1) the increase in transmission loss of high-frequency sound signal with depth is the key reason for the frequency-dependent attenuation of peak beams after beamforming in a VLA;
2) the attenuation rate of beam intensity is proportional to the array aperture, inversely proportional to the array deployment depth and source depth, and largely independent of the sound speed profile;
3) within a certain range, the M-MBIP method significantly outperforms the MBIP method in estimating source depth using a large-aperture VLA.

During data processing, it was observed that the replica envelope may exhibit a frequency shift relative to the data envelope. This phenomenon has the potential to impact the accuracy of source depth estimation methods. Additionally, the M-MBIP cannot be validated due to the lack of experimental data. Therefore, future research will focus on exploring the feasibility of target depth estimation under conditions of undersampling in the frequency domain of the sound field and verifying the effectiveness of the method with sea trial data.

Fundings

This work was supported by the National Natural Science Foundation of China, grant no. 12304501.

Conflict of interest

The authors declare that they have no known competing financial interests or personal relationships that could have appeared to influence the work reported in this paper.

Authors' contributions

Hao Wang conceptualized the study, performed the analysis, and wrote the original draft. Guangying Zheng performed the analysis and contributed to simulation data interpretation. Fangwei Zhu conceptualized the study and performed the analysis. Xiaohong Yang contributed to simulation data interpretation. Shuaishuai Zhang wrote the original draft. Xiaowei Guo performed the analysis. All authors reviewed and approved the final manuscript.

References

1. Duan R., Yang K., Li H., Ma Y. (2017), Acoustic–intensity striations below the critical depth: Interpretation and modeling, *The Journal of the Acoustical Society of America,* **142**(3): EL245 https://doi.org/10.1121/1.5000325.
2. Duan R., Yang K.D., Ma Y.L., Lei B. (2012), A reliable acoustic path: Physical properties and a source localization method, *Chinese Physics B*, **21**(12): 276–289, https://doi.org/10.1088/1674-1056/21/12/124301.
3. Gaul R.D., Knobles D.P., Shooter J.A., Wittenborn A.F. (2007), Ambient noise analysis of deep-ocean measurements in the northeast pacific, *IEEE Journal of Oceanic Engineering*, **32**(2): 497–512, https://doi.org/10.1109/JOE.2007.891885.
4. Kniffin G.P., Boyle J.K., Zurk L.M., Siderius M. (2016), Performance metrics for depth-based signal separation using deep vertical line arrays, *The Journal of the Acoustical Society of America*, **139**(1): 418–425, https://doi.org/10.1121/1.4939740.
5. Li H. *et al.* (2022), A multi-step method for passive broadband source localisation using a single vector sensor, *IET Radar, Sonar & Navigation*, **16**(10): 1656–1669, https://doi.org/10.1049/rsn2.12287.
6. Lei Z., Yang K., Ma Y. (2016), Passive localization in the deep ocean based on cross-correlation function matching, *The Journal of the Acoustical Society of America*, **139**(6): EL196, https://doi.org/10.1121/1.4954053.
7. McCargar R.K., Zurk L.M. (2012), Depth-based suppression of moving interference with vertical line arrays in the deep ocean, *The Journal of the Acoustical Society of America*, **132**(3_Supplement): 2081, https://doi.org/10.1121/1.4755682.
8. McCargar R., Zurk L.M. (2013), Depth-based signal separation with vertical line arrays in the deep ocean, *The Journal of the Acoustical Society of America*, **133**(4): EL320, https://doi.org/10.1121/1.4795241.
9. Porter M.B. (1991), *The KRAKEN Normal Mode Program*, ACLANT Undersea Research Centre, La Spezia, Italy.
10. Sun M., Zhou S.-H., Li Z.-L. (2016), Near-surface source localization in the direct-arrival zone in deep water using a deep-located vector sensor, *Chinese Science: Physics, Mechanics, Astronomy*, **46**(9): 094309, https://doi.org/10.1360/SSPMA2016-00080.
11. Wang W.B. *et al.* (2021), A broadband source depth estimation based on frequency domain interference pattern structure of vertical array beam output in direct zone of deep water [in Chinese], *Acta Acustica*, **46**(2): 161–170, https://doi.org/10.15949/j.cnki.0371-0025.2021.02.001.
12. Wei R., Ma X., Li X. (2020), Depth estimation of deep water moving source based on ray separation,

Applied Acoustics, **174**(2): 107739, https://doi.org/10.1016/j.apacoust.2020.107739.

13. Worcester P.F. *et al.* (2013), The North Pacific Acoustic Laboratory deep-water acoustic propagation experiments in the Philippine Sea, *The Journal of the Acoustical Society of America*, **134**(4): 3359–3375, https://doi.org/10.1121/1.4818887.

14. Xu Z., Li H., Lu D., Duan R., Yang K. (2023), Beam intensity resampling-based source depth estimation by using a vertical line array in deep water, *Applied Acoustics*, **211**: 109495, https://doi.org/10.1016/j.apacoust.2023.109495.

15. Zhang J.N., Fang E.Z., Wang H., Gui C. (2025), Target depth estimation based on matched broadband complex acoustic intensity by deep water vector vertical array [in Chinese], *Acta Acustica*, **50**(3): 677–692, https://doi.org/10.12395/0371-0025.2024001.

16. Zheng G.Y., Yang T.C., Ma Q., Du S. (2020), Matched beam intensity processing for a deep vertical line array, *The Journal of the Acoustical Society of America*, **148**(1): 347–358, https://doi.org/10.1121/10.0001583.

17. Zhou L., Zheng G.Y., Yang T.C. (2022), Target depth estimation by frequency interference matching for a deep vertical array, *Applied Acoustics*, **186**: 108493, https://doi.org/10.1016/j.apacoust.2021.108493.

18. Zhu F.W., Zheng G.Y., Liu F.C. (2021), Matched arrival pattern-based method for estimating source depth in deep water bottom bounce areas [in Chinese], *Journal of Harbin Engineering University*, **42**(10): 1510–1517, https://doi.org/10.11990/jheu.202007001.

19. Zhu Q., Sun C. (2023), Underwater source localisation utilising interference pattern under low SNR conditions, *IET Radar, Sonar & Navigation*, **17**(5): 876–887, https://doi.org/10.1049/rsn2.12384.